Green's function formulation for third-harmonic generation microscopy

Ji-Xin Cheng and X. Sunney Xie

Department of Chemistry and Chemical Biology, Harvard University, 12 Oxford Street, Cambridge, Massachusetts, 02138

Received July 18, 2001; revised manuscript received January 30, 2002

We report a theoretical study of third-harmonic generation (THG) microscopy by use of a Green's function formulation. The third-harmonic signal under a tight-focusing condition is calculated for samples with various shapes and sizes. Our results show that THG signals can be efficiently generated at a sizable interface perpendicular or parallel to the optical axis or from a small object with a size comparable to the width of the axial excitation intensity profile. The signal-generation mechanism of THG microscopy is explained by a modified phase-matching condition, $|\mathbf{k}_3 - 3(\mathbf{k}_1 + \Delta\mathbf{k}_g)|l \ll \pi$, where $\Delta\mathbf{k}_g$ is the wave vector mismatch induced by the Gouy phase shift of the focused excitation field. The relation of the THG power and radiation pattern to the orientation of an interface is investigated. A comparison between signal generation in THG microscopy and that in coherent anti-Stokes Raman scattering microscopy is given.

OCIS codes: 190.4160, 180.5810, 180.6900, 190.4380.

1. INTRODUCTION

The combination of nonlinear optical spectroscopy with scanning microscopy generates innovative tools such as second-harmonic generation microscopy,[1–3] coherent anti-Stokes Raman scattering (CARS) microscopy,[4–6] and third-harmonic generation (THG) microscopy[7–12] for biology and materials science. THG microscopy was demonstrated by Barad *et al.* in 1997.[7] This technique has been applied for imaging transparent objects,[7,8] laser-induced breakdown,[9] and biological samples.[10–12] The advantages of this technique are that it is capable of three-dimensional sectioning and that there is no need to stain the sample.

The theory of second-harmonic generation and THG by focused laser beams has been well established.[13,14] It was realized[14–17] that, with a focused excitation beam, THG from a homogenous bulk medium is canceled when the phase-matching condition is satisfied ($\mathbf{k}_3 - 3\mathbf{k}_1 = 0$, where $\mathbf{k}_3$ and $\mathbf{k}_1$ are the wave vectors of the third-harmonic field and the fundamental field). This interesting phenomenon was explained[17] as being a result of the Gouy phase shift[18] across the focus of the excitation beam. By using Boyd's two-dimensional model,[17] Barad *et al.* showed that third-harmonic signals can be generated at an interface that is perpendicular to the optical axis.[7]

In THG microscopy, one is interested in signals from small features of different sizes and shapes generated by a tightly focused excitation beam. Therefore previous studies of bulk media are inadequate to explain the imaging properties of THG microscopy. Moreover, the paraxial approximation that was used for describing focused laser beams previously is no longer valid under the tight-focusing condition.

In this paper we formulate THG microscopy with a Green's function method. The THG signal (image intensity at each pixel) is calculated as a coherent superposition of the third-harmonic radiation fields from induced dipoles inside a sample. This model permits three-dimensional calculation of nonlinear optical signal generation from a sample of arbitrary size and shape. The tightly focused laser beam is described by an angular spectrum representation.[19] Our results provide new insight into signal-generation mechanisms of THG microscopy.

2. THEORY

THG from a sample by a tightly focused laser beam is illustrated in Fig. 1. The sample in THG microscopy is usually heterogeneous, containing objects of interest and a surrounding medium. In our modeling we assume that the index mismatch between an object and its surrounding medium is negligible, so the distortion of the focal field can be neglected.[20]

Under the tight-focusing condition, the paraxial approximation no longer holds (see Appendix A). The focal field can be described by use of the angular spectrum representation. We assume that the excitation beam propagating along the z axis is linearly polarized along the x axis and focused by a lens with a focal length f, as shown in Fig. 1. The incident beam has a fundamental Gaussian profile:

$$E_{\mathrm{inc}}(\alpha) = E_0 \exp(-f^2 \sin^2 \alpha / w^2), \tag{1}$$

where w is the beam waist at the lens and α is in the range $[0, \alpha_{\max}]$. $\alpha_{\max}$ is the cone angle that is related to the numerical aperture (NA) of the lens and the refractive index (n) of the medium by $\alpha_{\max} = \sin^{-1}(\mathrm{NA}/n)$. The x-polarized component of the focal field can be described by[21,22]

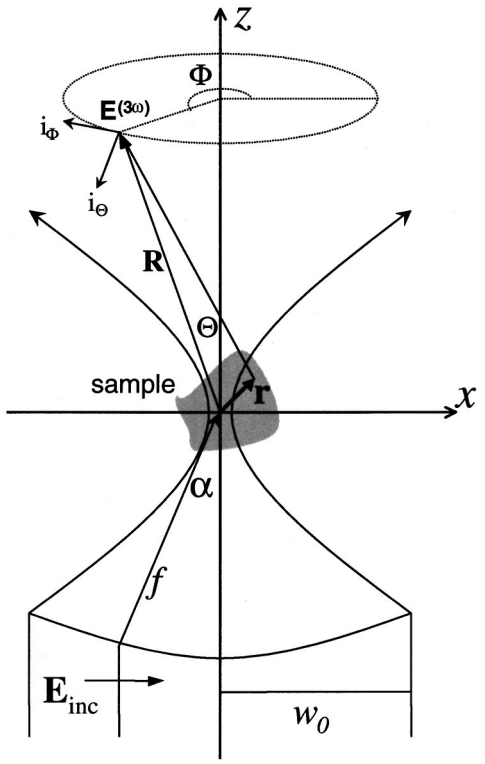

Fig. 1. Illustrations of THG by a focused laser beam with definitions of the parameters of the excitation and the THG fields.

$$E_{\text{foc}}(\rho, z) = ik_1 f \exp(-ik_1 f)/2 \int_0^{\alpha_{\max}} E_{\text{inc}} \sin\alpha \sqrt{\cos\alpha} \times (1 + \cos\alpha) J_0(k_1 \rho \sin\alpha) \times \exp(k_1 z \cos\alpha) \mathrm{d}\alpha, \quad (2)$$

with $\rho^2 = x^2 + y^2$. J_0 is the zero-order Bessel function. $k_1 = 2\pi n_1/\lambda_1$ is the wave-vector amplitude, and n_1 and λ_1 are the refractive index and the excitation wavelength, respectively. The y and z components of the focal field make much smaller contributions to THG than does the x component and is neglected in the following calculation.[23]

In a homogeneous system the third-harmonic signal field [$\mathbf{E}^{(3\omega)}$] is governed by the following wave equations under the slowly varying amplitude approximation[17]:

$$\nabla \times \nabla \times \mathbf{E}^{(3\omega)}(\mathbf{r}) - k_3^2 \mathbf{E}^{(3\omega)}(\mathbf{r}) = \frac{4\pi\omega_3^2}{c^2} \mathbf{P}^{(3\omega)}(\mathbf{r}). \quad (3)$$

Here, $\mathbf{P}^{(3\omega)}(\mathbf{r})$ is the induced nonlinear polarization at the third-harmonic frequency of ω_3. $k_3 = n_3\omega_3/c$ is the wave-vector amplitude and n_3 is the refractive index of the medium for the signal field. c is the velocity of light in vacuum. For an isotropic sample the induced third-order polarization in Eq. (3) is related to the focused laser excitation field by

$$P^{(3\omega)}(\mathbf{r}) = \chi^{(3)}(\mathbf{r}) E_{\text{foc}}(\mathbf{r}) E_{\text{foc}}(\mathbf{r}) E_{\text{foc}}(\mathbf{r}), \quad (4)$$

where $\chi^{(3)}(\mathbf{r})$ is the third-order susceptibility.

The exterior signal field detected at $\mathbf{R}(R, \Theta, \Phi)$ can be expressed in terms of the Green's function by[24]

$$\mathbf{E}^{(3\omega)}(\mathbf{R}) = -\frac{4\pi\omega_3^2}{c^2} \iiint_V dV \left(\mathbf{I} + \frac{\nabla\nabla}{k_3^2}\right) G(\mathbf{R} - \mathbf{r}) \cdot \mathbf{P}^{(3\omega)}(\mathbf{r}), \quad (5)$$

where $\mathbf{I}$ is a 3×3 unit matrix, V is the volume of the sample, and $G(\mathbf{R} - \mathbf{r}) = \exp(ik_3|\mathbf{R} - \mathbf{r}|)/(4\pi|\mathbf{R} - \mathbf{r}|)$ is the scalar Green's function. For far-field radiation ($|\mathbf{R}| \gg |\mathbf{r}|$), $|\mathbf{R} - \mathbf{r}|$ can be approximated as $|\mathbf{R}| - \mathbf{R} \cdot \mathbf{r}/|\mathbf{R}|$. The signal field can be recast as[25]

$$\mathbf{E}^{(3\omega)}(\mathbf{R}) = -\frac{\omega_3^2}{c^2} \frac{\exp(ik_3|\mathbf{R}|)}{|\mathbf{R}|} \iiint_V \mathrm{d}V \exp\left(\frac{-ik_3 \mathbf{R} \cdot \mathbf{r}}{|\mathbf{R}|}\right) \times \begin{bmatrix} 0 & 0 & 0 \\ \cos\Theta\cos\Phi & \cos\Theta\sin\Phi & -\sin\Theta \\ -\sin\Phi & \cos\Phi & 0 \end{bmatrix} \times \begin{bmatrix} P_x^{(3\omega)}(\mathbf{r}) \\ P_y^{(3\omega)}(\mathbf{r}) \\ P_x^{(3\omega)}(\mathbf{r}) \end{bmatrix} \begin{matrix} \hat{i}_R \\ \hat{i}_\Theta \\ \hat{i}_\Phi \end{matrix}. \quad (6)$$

Here $\hat{i}_R$, $\hat{i}_\Theta$, and $\hat{i}_\Phi$ are unit vectors that represent the spherical components of the signal field. The above formulation can be extended to any nonlinear optical signal generation. We have used a similar formulation for CARS microscopy.[5] We assume that the signal is collected with a second lens of the same NA in the forward direction. We calculate the third-harmonic power by integrating the third-harmonic field intensity over a spherical surface of radius R within the cone angle of the objective lens ($0 < \Theta < \alpha_{\max}$, $0 < \Phi < 2\pi$):

$$P^{(3\omega)} = \frac{n_3 c}{8\pi} \int_0^{\alpha_{\max}} \mathrm{d}\Theta \int_0^{2\pi} \mathrm{d}\Phi |\mathbf{E}^{(3\omega)}(\mathbf{R})|^2 \mathbf{R}^2 \sin\Theta. \quad (7)$$

3. RESULTS AND DISCUSSION

In the calculation we assume that (i) both the focusing and the collecting objectives have the same NA, 1.4, (ii) the incident beam waist matches the back aperture of the objective lens ($w = f \sin\alpha_{\max}$), and (iii) there is no dispersion of the refractive index ($n_1 = n_3 = 1.5$).[26] We first consider a spherical sample centered at the focus. The dependence of the integrated THG signal calculated by Eq. (7) on the diameter (D) of the sphere is plotted in Fig. 2. The THG signal increases with the sample size initially and reaches its maximum at $D = 0.7\lambda_1$. Then the signal is gradually attenuated as the diameter increases further and becomes negligible for a bulk sample. The angular distribution of the THG power under the tight-focusing condition is calculated with Eq. (6). Figures 3(a) and 3(b) display the radiation patterns for a small sphere ($D = 1.0\lambda_1$) centered at the focus and at ($x = 0.5\lambda_1$, $y = 0$, $z = 0$), respectively. In both cases the THG signal exhibits a sharp radiation pattern along the optical axis in the forward direction, with little signal going backward. The THG power shows an obvious dependence on Φ when the laser beam is focused on the edge of such a $D = 1.0\lambda_1$ sphere [Fig. 3(b)]. Our calculations imply that a low-NA condenser lens with a long working dis-

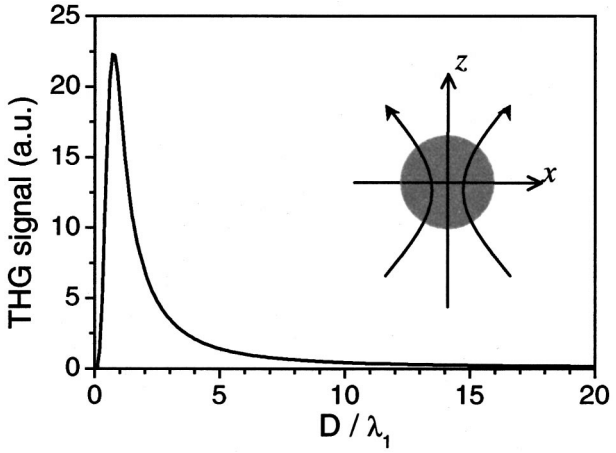

Fig. 2. Integrated THG signal as a function of the diameter (D) of a spherical sample centered at the focus of a tightly focused (NA = 1.4) excitation beam.

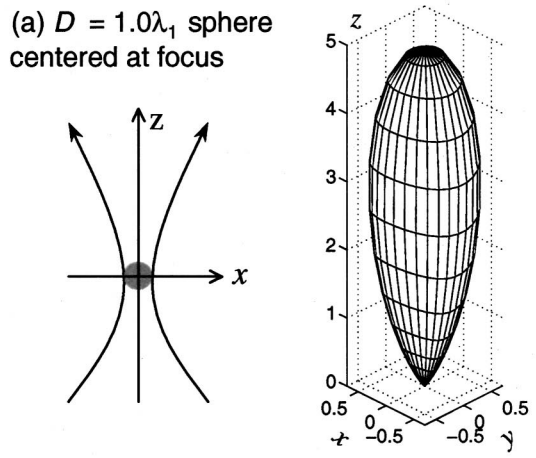

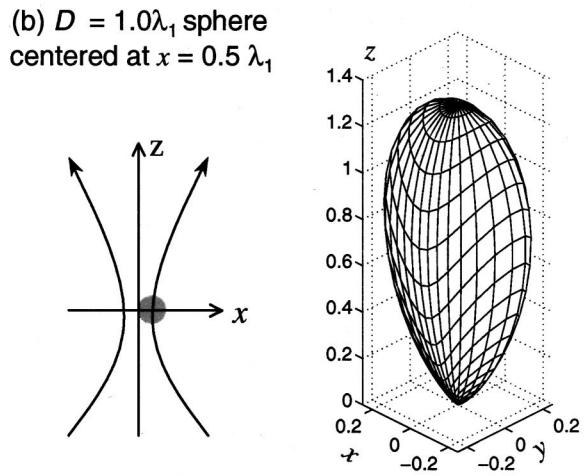

Fig. 3. (a) Far-field radiation pattern of THG from a $D = 1.0\,\lambda_1$ sphere centered at the focus. (b) Far-field radiation pattern of THG from a $D = 1.0\,\lambda_1$ sphere centered at ($x = 0.5\,\lambda_1, y = 0, z = 0$). The x, y, and z axes have the same scale, with arbitrary units.

tance is enough for efficient collection of THG signals generated from small objects. This brings practical convenience for THG imaging.

Third-harmonic generation from an interface perpendicular to the optical axis was illustrated by Barad *et al.*[7] With the Green's function model we are able to investigate THG from interfaces of different orientations. Figure 4 shows that THG signals can arise from an interface perpendicular or parallel to the optical axis. Interestingly, the THG signal is dependent on the polarization direction of the excitation beams. The signal from an interface parallel to the polarization of the excitation field along the x axis (case B) is slightly larger than that from an interface perpendicular with the excitation polarization (case C).

Figure 5 displays the radiation patterns of THG from interfaces perpendicular and parallel to the optical axis. The THG signal from an interface perpendicular to the optical axis displays a sharp radiation pattern that is maximized along the optical axis [Fig. 5(a)]. For an interface that is perpendicular to the x axis the radiation maximum is deflected from the optical axis by 26° [Fig. 5(b)]. Moreover, the THG signal shows a strong dependence on Φ, with two radiation power maxima at $\Phi = 0°, 180°$. For an interface perpendicular to the y axis the deflection angle is calculated to be 28°, and the two radiation power maxima appear at $\Phi = 90°, 270°$ (not shown). Thus, under the tight-focusing (NA = 1.4) condition, a lens with NA/n larger than 0.47 is necessary for efficient collection of the THG signal from an interface that is parallel to the optical axis. The deflection of the THG radiation maximum from the optical axis could explain the report in a previous paper[8] that little signal was detected from an interface parallel with the optical axis, where the THG signal generated by an NA = 0.45 objective was deflected by an angle of 14° and was along the edge of the collection cone of an NA = 0.25 objective.

The calculation above does not include the signal from the surrounding medium. For an object embedded in a nonlinear medium or a sizable interface of two media the THG field detected at $\mathbf{R}$ is a superposition of the third-harmonic radiation fields from the object and from the solvent medium:

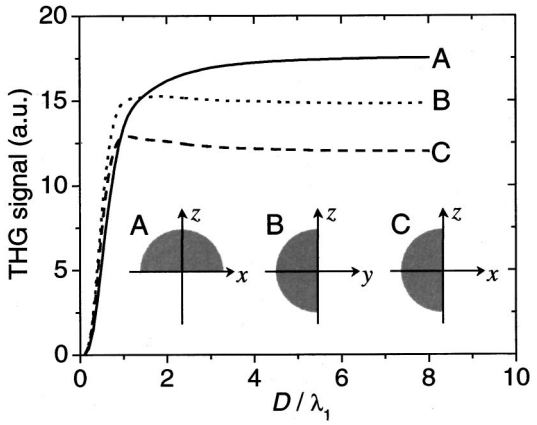

Fig. 4. Integrated THG signal from hemispherical samples as a function of diameter (D). The samples are centered at the focus and symmetric with respect to the z (solid curve), x (dotted curve), and y (dashed curve) axes. The polarization of the excitation field is along the x axis.

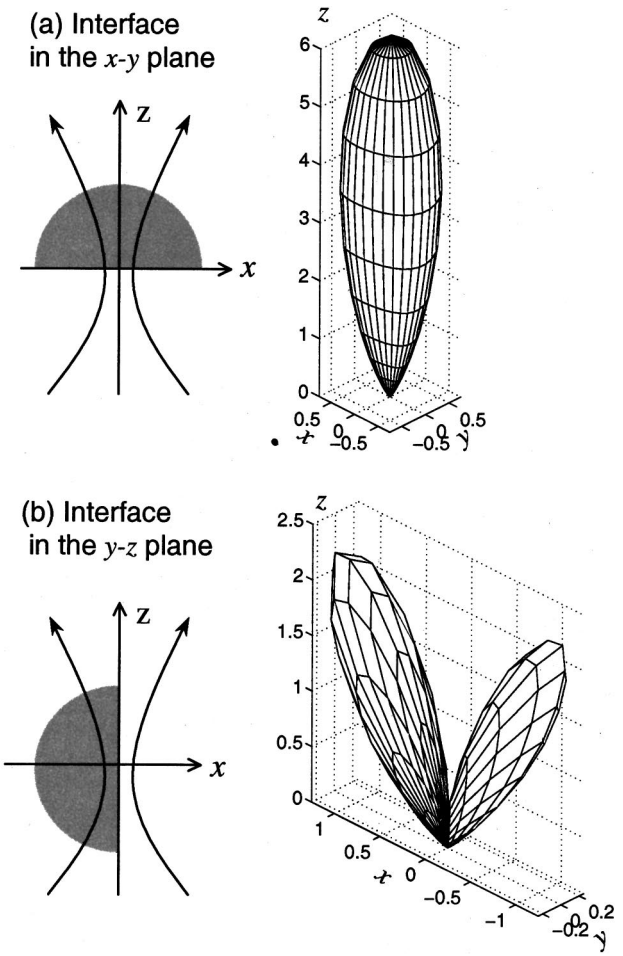

Fig. 5. (a) Far-field radiation pattern of THG from a $D = 6.0\,\lambda_1$ hemisphere centered at the focus and perpendicular to the optical axis. (b) Far-field radiation pattern of THG from a $D = 6.0\,\lambda_1$ hemisphere centered at the focus and perpendicular to the x axis. The x, y, and z axes have the same scale, with arbitrary units. The polarization of the excitation field is along the x axis.

$$\mathbf{E}^{\mathrm{THG}}(\mathbf{R}) = \int\int\int_V \mathbf{E}^{\mathrm{THG}}[\mathbf{R},\mathbf{r},\chi^{(3)}_{\mathrm{obj}}]\mathrm{d}V + \int\int\int_{V'} \mathbf{E}^{\mathrm{THG}}[\mathbf{R},\mathbf{r},\chi^{(3)}_{\mathrm{sol}}]\mathrm{d}V', \qquad (8)$$

where V and V' denote the volume occupied by the object and the solvent, respectively. $\chi^{(3)}_{\mathrm{obj}}$ and $\chi^{(3)}_{\mathrm{sol}}$ denote the third-order susceptibility of the object and of the solvent, respectively. Because the radiation field from a bulk solvent $(V + V')$ is negligible, we have

$$\mathbf{E}^{\mathrm{THG}}(\mathbf{R}) = \int\int\int_V \mathbf{E}^{\mathrm{THG}}[\mathbf{R},\mathbf{r},\chi^{(3)}_{\mathrm{obj}}]\mathrm{d}V - \int\int\int_V \mathbf{E}^{\mathrm{THG}}[\mathbf{R},\mathbf{r},\chi^{(3)}_{\mathrm{sol}}]\mathrm{d}V = \int\int\int_V \mathbf{E}^{\mathrm{THG}}[\mathbf{R},\mathbf{r},\chi^{(3)}_{\mathrm{obj}} - \chi^{(3)}_{\mathrm{sol}}]\mathrm{d}V. \qquad (9)$$

Equation (9) indicates that the THG signal from an object that has $\chi^{(3)}_{\mathrm{obj}}$ embedded in a nonlinear medium with $\chi^{(3)}_{\mathrm{sol}}$ obeys the same size dependence and radiation pattern but with an effective sample susceptibility of $\chi^{(3)}_{\mathrm{obj}} - \chi^{(3)}_{\mathrm{sol}}$. As a result, a small vacuum hole in a nonlinear medium (e.g., laser-induced breakdown[9]) is equivalent to an object with $-\chi^{(3)}_{\mathrm{sol}}$ and can be detected with THG microscopy.

We can qualitatively interpret the size dependence and the radiation pattern of the THG signal shown in Figs. 2–5 by considering the Gouy phase shift of the focal field. The THG signal results from a coherent superposition of the radiation field from each induced dipole inside a sample. The Gouy phase shift of the excitation field contributes a spatially dependent phase factor to the induced dipoles and consequently affects the coherent superposition of the third-harmonic radiation fields. We present a modified phase-matching condition for THG with a focused laser beam:

$$|(\mathbf{k}_3 - 3\mathbf{k}_1) - 3\Delta\mathbf{k}_g|l \ll \pi, \qquad (10)$$

where $\Delta\mathbf{k}_g$ is the wave vector mismatch induced by the Gouy phase shift of the focused excitation field and is directed along the axial $(+z)$ direction. For a small object centered at the focus, the interaction length (l) is the axial length of the object. For simplicity, we consider the axial direction $(\Theta = 0)$, and inequality (10) can be recast as $(\mathbf{k}_3 - 3\mathbf{k}_1)l - 3\Delta\mathbf{k}_g l \ll \pi$. $(\mathbf{k}_3 - 3\mathbf{k}_1)l$ arises from the dispersion of the refractive index and becomes negligible under the tight-focusing condition.[26] To evaluate the effect of the Gouy phase shift we calculated the axial phase shift and intensity distribution of the focal field generated by an NA = 1.4 lens by using Eq. (2); the results are shown in Fig. 6. The $[-0.8\lambda_1, 0.8\lambda_1]$ region where the major THG signal is generated exhibits a nearly linear and negative phase shift of $-0.8\,\pi$. For a THG process, this phase shift generates a negative wave-vector mismatch of $-3\Delta k_g = 2.4\pi/1.6\lambda_1$, corresponding to a coherence length of $\pi/(-3\Delta k_g) = 0.7\lambda_1$. The coherence length is the maximum interaction length within which the coherent addition of the signal field is constructive. Under the tight-focusing (NA = 1.4) condition, the estimated coherence length $(0.7\lambda_1)$ matches the sphere diameter of $0.7\lambda_1$ where the maximum THG signal appears (Fig. 2). In general, the maximal signal for a spherical sample centered at the focus appears when the sphere's diameter is near the FWHM of the axial excitation intensity profile.

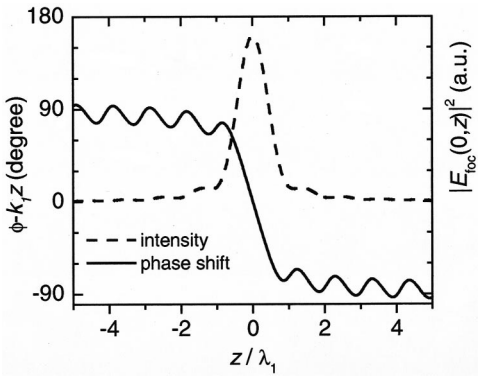

Fig. 6. Axial phase shift and intensity distribution in the focal region of a Gaussian beam focused by an objective lens with an NA of 1.4.

When the spheres diameter exceeds the coherence length, the phase mismatch induced by the Gouy phase shift causes destructive interference of the THG radiation from the various parts of the sample. This interference results in a decreasing THG signal (Fig. 2) and eventually a vanishing of the signal from a bulk sample, as demonstrated previously.[14–17] For a semi-infinite sample located in the $z > 0$ region the coherence length ($0.7\lambda_1$) associated with the Gouy phase shift is comparable with the axial length of the region ($0 < z < 0.8\lambda_1$), where the major THG signal is generated from such a semi-infinite sample with no destructive interference. This explains the efficient THG from an interface perpendicular to the optical axis.

For an interface that is parallel to the optical axis, the effect of the Gouy phase shift is to deflect the phase-matching direction, i.e., the radiation maximum, off the optical axis. For an interface located in the y–z plane the deflection angle (Θ_d) in the x–z plane ($\Phi = 0$) can be estimated with the modified phase-matching condition [inequality (10)]. Under the phase-matching condition we have $(k_3 - 3k_1) + k_3(\cos\Theta_d - 1) - 3\Delta k_g = 0$ for the axial direction; the first term can be neglected.[26] With $\Delta k_g = -0.8\pi/1.6\lambda_1$, Θ_d is calculated to be 33°, close to our three-dimensional calculation shown in Fig. 5(b). A similar effect of the Gouy phase shift on second-harmonic generation microscopy has been shown for a two-dimensional sample parallel with the optical axis.[3]

It is interesting to compare signal generation in THG microscopy with that in CARS microscopy.[4–6,27] CARS is another four-wave mixing process with $P^{(3)} = \chi^{(3)}E_1E_2^*E_1$. The effect of the Gouy phase shift is partially canceled in CARS by the interaction of the pump field (E_1) with the conjugate Stokes field (E_2^*). Under the same tight-focusing condition, the wave-vector mismatch associated with the Gouy phase shift is roughly $0.8\pi/1.6\lambda_1$, corresponding to a coherence length of $2\lambda_1$. Therefore the coherent addition of the CARS fields is constructive within the $[-1.0\lambda_1, 1.0\lambda_1]$ region (see Fig. 6) where the major CARS signal is generated. Consequently there is a large CARS signal from a bulk sample. Epidetection has been used in CARS microscopy to suppress the resonant and nonresonant CARS signals from a bulk solvent.[5,27] The epidetection geometry introduces a wave-vector mismatch that corresponds to a small coherence length. Thus, epidetected CARS microscopy possesses a signal-generation mechanism similar to that of THG microscopy. However, epidetection is not necessary for THG microscopy because of cancellation of the signal from a bulk sample in the forward direction.

We shall end the discussion with a calculation of image formation in THG microscopy. For each pixel in a THG image, the integration in Eq. (6) is over a spherical volume centered at the focus with a diameter of $6.0\,\lambda_1$. The relation between the third-order susceptibility of the object and that of the solvent is assumed to be $\chi^{(3)}_{\text{obj}} = 2\chi^{(3)}_{\text{sol}}$. Figures 7(a) and 7(b) show the calculated THG intensity profiles of a $D = 0.5\lambda_1$ spherical sample centered on and scanned along the x and z axes, respectively. The criterion for signal generation from such a small object is that the size of the object be smaller than the coherence length associated with the Gouy phase shift.

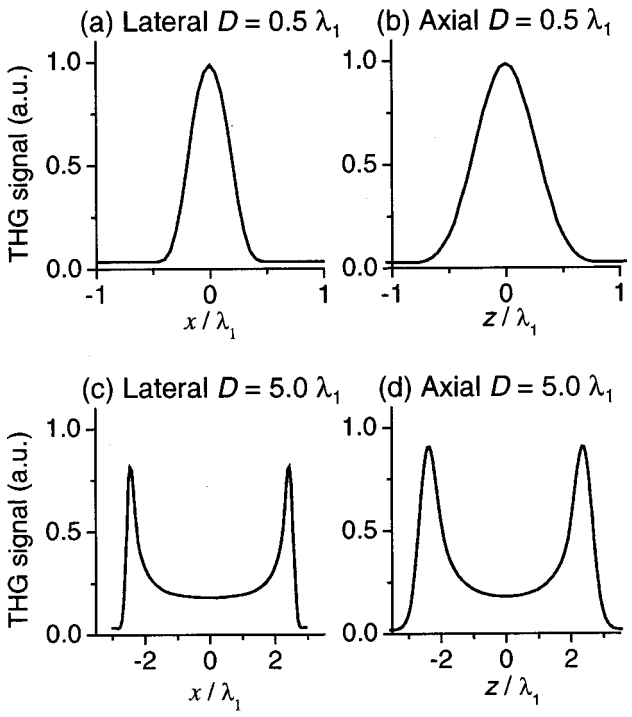

Fig. 7. (a), (b) Calculated lateral (x) and axial (z) THG intensity profiles of a $D = 0.5\,\lambda_1$ spherical sample embedded in a nonlinear medium. (c), (d) Calculated lateral (x) and axial (z) THG intensity profiles of a $D = 5.0\,\lambda_1$ spherical sample embedded in a nonlinear medium.

That this is so can be seen from the axial and lateral peak positions that are located at the center of the sphere. Our result explains the observed high signal-to-background ratio of intracellular organelles in the THG images.[11] Figures 7(c) and 7(d) show the calculated THG intensity profiles of a $D = 5.0\lambda_1$ spherical sample centered on and scanned along the x and z axes, respectively. For such a large object, the signal is generated mainly at the boundary, and the intensity depends on the orientation of the interface (cf. Fig. 4). This result is consistent with the observation in THG imaging of a large glass sphere.[10] The lateral and depth resolution of THG microscopy can be estimated from the FWHM of the lateral and axial intensity profiles along a small object (e.g., a $D = 0.2\lambda_1$ sphere), which are calculated to be $0.3\lambda_1$ and $0.6\lambda_1$, respectively.

4. CONCLUSION

We have studied signal generation in THG microscopy by using a Green's function formulation. This model permits calculation of nonlinear optical signals from a three-dimensional object of any shape and size. The signal-generation mechanisms are interpreted with a modified phase-matching condition, $|\mathbf{k}_3 - 3(\mathbf{k}_1 + \Delta\mathbf{k}_g)|l \ll \pi$, where $\Delta\mathbf{k}_g$ is the wave-vector mismatch induced by the Gouy phase shift of the focused excitation field. Third-harmonic signals can be efficiently generated from a sizable interface or from a small object with a size comparable to the FWHM of the axial excitation intensity profile. The signal from a bulk medium is canceled by a wave-vector mismatch associated with the Gouy phase

shift of the focused excitation field. This permits THG imaging of small features with a high signal-to-background ratio. The THG radiation from a small object or an interface perpendicular to the optical axis exhibits a sharp radiation pattern along the optical axis in the forward direction. For an interface parallel to the optical axis, the role of the Gouy phase shift is to deflect the phase-matching direction, i.e., the THG radiation maximum direction, off the optical axis.

APPENDIX A

We compare the calculation of THG signals with the paraxial approximation and that with the angular spectrum representation under the tight-focusing condition. Under the paraxial approximation the focal field for a fundamental Gaussian excitation beam is described as

$$E_{\mathrm{foc}}(\rho, z) = E_0 \frac{w_0}{w(z)} \exp\left[-\frac{\rho^2}{w(z)^2}\right] \exp\{i[k_1 z - \eta(z) + k_1 \rho^2/2R(z)]\}, \tag{A1}$$

where $w(z) = w_0(1 + z^2/z_0^2)^{1/2}$ is the beam radius. $R(z) = z(1 + z_0^2/z^2)^{1/2}$ is the wave-front radius. $\eta(z) = \arctan(z/z_0)$ is the Gouy phase shift. $z_0 = k_1 w_0^2/2$ is the Rayleigh range. w_0 is the beam waist radius at the focus and is calculated as $0.61\lambda_1/(\mathrm{NA}\sqrt{2 \ln 2})$, with NA = 1.4. A comparison of the integrated THG power from a sphere centered at the focus calculated with Eq. (A1) and that calculated with Eq. (2) is shown in Fig. 8. For both methods the THG signal vanishes for a bulk sample, consistent with the analytical results presented previously.[17] However, the maximum signal appears at $D = 1.4\lambda_1$ under the paraxial approximation, and it appears at $D = 0.7\lambda_1$ for the angular spectrum representation. This discrepancy results from neglect of the high-order terms in the field expansion under the paraxial approximation. Although the y- and z-polarized components can be neglected in the calculation of nonlinear signal generation, the x-polarized component is poorly described under the paraxial approximation.

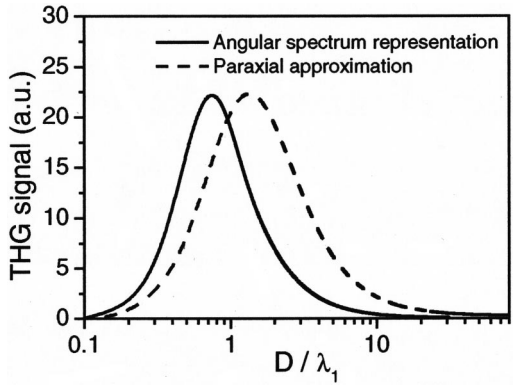

Fig. 8. THG signal as a function of diameter (D) for a spherical sample centered at the focus, generated with a tightly focused (NA = 1.4) excitation field calculated by Eq. (2) (solid curve) and by Eq. (A1) (dashed curve).

ACKNOWLEDGMENTS

This study was supported by National Institutes of Health grant GM62536-01. The authors thank L. Novotny for sharing Eq. (2).

X. S. Xie's email address is xie@chemistry.harvard.edu.

REFERENCES AND NOTES

1. R. Gauderon, P. B. Lukins, and C. J. R. Sheppard, "Three-dimensional second-harmonic generation imaging with femtosecond laser pulses," Opt. Lett. **23**, 1209–1211 (1998).
2. P. J. Campagnola, M.-D. Wei, A. Lewis, and L. M. Loew, "High-resolution nonlinear optical imaging of live cells by second harmonic generation," Biophys. J. **77**, 3341–3349 (1999).
3. L. Moreaux, O. Sandre, and J. Mertz, "Membrane imaging by second-harmonic generation microscopy," J. Opt. Soc. Am. B **17**, 1685–1694 (2000).
4. A. Zumbusch, G. R. Holtom, and X. S. Xie, "Three-dimensional vibrational imaging by coherent anti-Stokes Raman scattering," Phys. Rev. Lett. **82**, 4142–4145 (1999).
5. A. Volkmer, J.-X. Cheng, and X. S. Xie, "Vibrational imaging with high sensitivity via epidetected coherent anti-Stokes Raman scattering microscopy," Phys. Rev. Lett. **87**, 023901 (2001).
6. J. X. Cheng, L. D. Book, and X. S. Xie, "Polarization coherent anti-Stokes Raman scattering microscopy," Opt. Lett. **26**, 1341–1343 (2001).
7. Y. Barad, H. Eisenberg, M. Horowitz, and Y. Silberberg, "Nonlinear scanning laser microscopy by third-harmonic generation," Appl. Phys. Lett. **70**, 922–924 (1997).
8. M. Müller, J. Squier, K. R. Wilson, and G. J. Brakenhoff, "3D microscopy of transparent objects using third-harmonic generation," J. Microsc. (Oxford) **191**, 266–274 (1998).
9. J. A. Squier and M. Muller, "Third-harmonic generation imaging of laser-induced breakdown in glass," Appl. Opt. **38**, 5789–5794 (1999).
10. J. A. Squier, M. Muller, G. J. Brakenhoff, and K. R. Wilson, "Third harmonic generation microscopy," Opt. Express **3**, 315–324 (1998), http://www.opticsexpress.org.
11. D. Yelin and Y. Silberberg, "Laser scanning third-harmonic-generation microscopy in biology," Opt. Express **5**, 169–175 (1999), http://www.opticsexpress.org.
12. L. Canioni, S. Rivet, L. Sarger, R. Barille, P. Vacher, and P. Voisin, "Imaging Ca^{2+} intracellular dynamics with a third-harmonic generation microscope," Opt. Lett. **26**, 515–517 (2001).
13. D. A. Kleinman, A. Ashkin, and G. D. Boyd, "Second-harmonic generation of light by focused laser beams," Phys. Rev. **145**, 338–379 (1966).
14. J. F. Ward and G. H. C. New, "Optical third harmonic generation in gases by a focused laser beam," Phys. Rev. **185**, 57–72 (1969).
15. G. C. Bjorklund, "Effects of focusing on third-order nonlinear processes in isotropic media," IEEE J. Quantum Electron. **QE-11**, 287–296 (1975).
16. R. B. Miles and S. E. Harris, "Optical third-harmonic generation in alkali metal vapors," IEEE J. Quantum Electron. **QE-9**, 470–484 (1973).
17. R. W. Boyd, *Nonlinear Optics* (Academic, Boston, Mass., 1992).
18. A. E. Siegman, *Lasers* (University Science, Mill Valley, Calif. 1986).
19. M. Born and E. Wolf, *Principles of Optics*, 7th ed. (Cambridge U. Press, Cambridge, 1999).
20. The effect of distortion is quite small when the laser beam is focused on small features. The discontinuity of $\chi^{(1)}$ (refractive index) at a sizable interface provides an additional mechanism for THG signal generation.
21. B. Richards and E. Wolf, "Electromagnetic diffraction in optical systems. II. Structure of the image field in an

aplanatic system," Proc. R. Soc. London, Ser. A **253**, 358–379 (1959).
22. L. Novotny, *Lecture Notes on Nano-Optics* (University of Rochester, Rochester, N.Y., 2000).
23. For a fundamental Gaussian beam, $\max[E_y^2]/\max[E_x^2] = 0.003$ and $\max[E_z^2]/\max[E_x^2] = 0.12$ under the tight-focusing (NA = 1.4) condition. As THG is a third-order nonlinear process, the contributions from the y and z components are negligible. For the same reason, the azimuth-dependent part of the x-polarized component can be neglected.
24. W. C. Chew, *Waves and Fields in Inhomogeneous Media*, 2nd ed. (Institute of Electrical and Electronics Engineers, New York, 1995).
25. L. Novotny, "Allowed and forbidden light in near-field optics. II. Interacting dipolar particles," J. Opt. Soc. Am. A **14**, 105–113 (1997).
26. The effect of index dispersion on the phase mismatch can be neglected because of the small excitation volume under the tight-focusing condition. For example, the refractive index of water is 1.339 at 0.4 μm and 1.324 at 1.2 μm. The corresponding coherence length, $\pi/|\mathbf{k}_3 - 3\mathbf{k}_1|$, is calculated to be 13.3 μm, which is much larger than the axial length of the focal volume under the tight-focusing condition.
27. J. X. Cheng, A. Volkmer, L. D. Book, and X. S. Xie, "An epi-detected coherent anti-Stokes Raman scattering (E-CARS) microscope with high spectral resolution and high sensitivity," J. Phys. Chem. B **105**, 1277–1280 (2001).